

# Resolving Three-Dimensional Nanoscale Heterogeneities in Lithium Metal Batteries with Cryogenic Electron Tomography

Zewen Zhang,<sup>1,†</sup> Yanbin Li,<sup>1,†</sup> Weijiang Zhou,<sup>2,†</sup> Gong-Her Wu,<sup>3</sup> Jane Kristina Jiahui Lee,<sup>4</sup> Jiayu Wan,<sup>1</sup> Hao Chen,<sup>1</sup> William Huang,<sup>1</sup> Yusheng Ye,<sup>1</sup> Michael F. Schmid,<sup>5</sup> Wah Chiu,<sup>2,3,5,\*</sup> and Yi Cui<sup>1,6,7\*</sup>

<sup>1</sup> Department of Materials Science and Engineering, Stanford University, Stanford, CA 94305, USA.

<sup>2</sup> Biophysics Program, School of Medicine, Stanford University, Stanford, CA 94305, USA

<sup>3</sup> Department of Bioengineering, Stanford University, Stanford, CA 94305, USA

<sup>4</sup> Department of Structural Biology, Stanford Medicine, Stanford, CA 94305, USA

<sup>5</sup> Division of CryoEM and Bioimaging, SSRL, SLAC National Accelerator Laboratory, Menlo Park, CA, 94025, USA

<sup>6</sup> Stanford Institute for Materials and Energy Sciences, SLAC National Accelerator Laboratory, 2575 Sand Hill Road, Menlo Park, CA 94025, USA.

<sup>7</sup> Department of Energy Science and Engineering, Stanford University, Stanford, CA 94305, USA.

<sup>†</sup> These authors contributed equally: Zewen Zhang, Yanbin Li, Weijiang Zhou

\*Correspondence and requests for materials should be addressed to Wah Chiu (email: wahc@stanford.edu) and Yi Cui (email: yicui@stanford.edu)

## ABSTRACT

Current direct observation of sensitive battery materials and interfaces primarily relies on two-dimensional (2D) imaging, leaving out their three-dimensional (3D) relationship. Here, we used cryogenic electron tomography (cryo-ET) to visualize the lithium metal anode in 3D at nanometer resolution and cryogenic electron microscopy (cryo-EM) to reveal atomic details in local regions. We imaged both freshly prepared and calendar aged Li metal anodes to reveal the development of LiH in Li dendrites and the Li-LiH interface, as well as the development of the solid-electrolyte interphase (SEI). Using a convolutional neural network-based technique, the 3D arrangement of Li metal, along with nanoscale LiH and Cu heterogeneities in dendrites were visualized and annotated. In longer-term calendar aging, we observed more substantial LiH growth accompanied by extended SEI growth. Our results show that the growth of LiH and of the extended SEI during battery calendar aging are temporally and spatially separate processes.

**KEYWORDS:** lithium-metal battery, lithium hydride, solid-electrolyte interphase, cryogenic electron tomography, anode intraparticle heterogeneity

## INTRODUCTION

Nanoscale inhomogeneities build up in electrode particles during cycling, and decrease the reversibility of the battery reactions<sup>1,2</sup>. Both the irreversible structural damage in individual electrode particles, for example the fracturing of Si negative electrodes<sup>3–5</sup>, and the formation of electrochemically inactive species, for example the formation of the solid-electrolyte interphase (SEI)<sup>6,7</sup>, lead to the irreversible loss of active materials and depletion of the usable lithium inventory and electrolyte<sup>8</sup>. Resolving the three dimensional (3D) spatial distribution of heterogeneous degradation at the single electrode particle level with nanometer resolution can shed light into battery degradation pathways and their reaction kinetics, leading to the development of new materials and strategies for improved battery performance.

One critical problem regarding the cycling stability of batteries in commercial cell formats (limited dead volume), like pouch cells, is battery swelling<sup>9–11</sup>. Multiple aspects contribute to the overall swelling, including electrode stack swelling and gaseous swelling<sup>9,12</sup>. On one hand, SEI builds up upon fracture and growth during repetitive cycling and calendar aging<sup>13</sup>. On the other hand, the accumulation of gaseous byproducts, such as hydrogen gas, poses a significant risk to battery structural integrity as well as to safety due to their inherent flammability<sup>14,15</sup>. Moreover, these gaseous species can potentially react with the electrode to cause loss of lithium inventory<sup>16</sup>. For example, Li metal anode was hypothesized to react with hydrogen to form LiH during cycling<sup>17</sup>.

The existence of LiH and its formation mechanism in Li metal anodes are still poorly understood, partly due to the difficulty in direct observation of environmentally reactive and electron beam sensitive lithium metal and SEI<sup>18,19</sup>. Aurbach and colleagues first proposed the possibility of hydrogen reacting at the Li metal anodes to generate LiH<sup>17</sup>. In 2017, Cui and colleagues reported the first atomic resolution image Li metal lattice and SEI enabled by cryo-EM<sup>20</sup>. In 2018, Kourkoutis and colleagues used cryogenic scanning transmission electron microscopy (cryo-STEM) electron energy loss spectroscopy (EELS) to directly identify the existence of LiH in Li metal anodes based on H and Li K-edges<sup>21</sup>. In 2021, Wang and colleagues reported the existence of LiH in SEI with XRD characterization on cycled SEI in Li metal batteries<sup>22</sup>. Despite reports on LiH formation in the Li metal anodes<sup>17,21–24</sup>, little is known about where and when LiH is formed. There are hypotheses suggesting that hydrogen, as a byproduct of SEI formation and growth, may contribute to the growth of LiH in Li metal anodes. Therefore, bridging the gap in understanding interfacial reactions between Li metal anode, its SEI, and corresponding LiH formation bears great significance.

Current direct observations of the SEI and Li metal are largely based on the two-dimensional imaging techniques, where the 3D spatial relationships are undetermined. Transmission X-ray microscopy (TXM) is widely used to perform nano-computed-tomography (nano-CT) for energy science<sup>25–27</sup>, especially for Li-ion batteries<sup>25,28–30</sup>. One main advantage of imaging by X-ray CT over other techniques is that it is non-destructive. However, a typical nano-CT can practically

reach a resolution of only 30-60 nm<sup>31</sup>. While it is suitable for electrode-level structural characterization, the resolution falls short of providing sufficient details to delineate subparticle heterogeneity. Specifically, the diameters of Li metal dendrites are on the order of a few hundred nanometers and SEI is typically tens of nanometers, which correspond to a few or even less than one pixel in an X-ray CT image. In addition, X-ray tomography is less ideal for light elements like H and Li due to less X-ray absorption and low contrast in projection images. On the contrary, electron tomography works well with light elements and can reach subnanometer resolution in TEM<sup>32,33</sup>.

Herein, we demonstrate for nanometer resolution imaging of 3D structure of freshly deposited and aged Li metal anode materials by leveraging the recent development of cryo-EM and cryo-ET, which leads to new findings. In calendar aging, two different phenomena were observed: the growth of LiH and the growth of extended SEI<sup>21,34,35</sup>. In short term calendar aging, we only observed the growth of LiH in Li metal anodes. In longer term calendar aging, there was more extensive LiH and extended SEI growth, preferentially associated with the Li metal portion rather than LiH portion of the dendrite. While we cannot rule out other possibilities, the observation that the majority of extended SEI is on the Li metal portion in the dendrite indicates that the growth of extended SEI was largely localized to the Li metal surface.

The findings of temporal and spatial separations in LiH growth and extended SEI growth lead to our conclusion that there are two distinct pathways to LiH growth and extended SEI growth. Our multiscale imaging provides a link between individual compositions in the materials and their structural contexts to yields a better understanding of distinct aging modes in Li metal anodes to inform mitigation strategies to optimize Li metal batteries.

## RESULTS AND DISCUSSION

Lithium metal deposition was carried out in a commercial carbonate electrolyte, 1M LiPF<sub>6</sub> in ethylene carbonate (EC)/diethylene carbonate (DEC). Freshly deposited Li metal, half-stripped Li metal, and calendar aged Li metal samples were prepared. The cryo-EM sample preparation and transfer procedures followed the previous report<sup>36</sup> and details can be found in the Methods section. To obtain a tomogram of the object of interest in cryo-ET, a series of projection images was taken between  $\pm 60^\circ$  at an angular increment of  $1^\circ$  under a dose-symmetric scheme. The projection image series will then be pre-processed and aligned to be ready for tomogram reconstruction. The computational reconstruction can be carried out with the available algorithms, for example the weighted back-projection method<sup>37</sup> (**Fig. 1a**). Of note, for tomography, it is preferred that the Li metal dendrites sit in the same direction as the tilting axis of the microscope to maximize the spatial information of the tomograms. Thus, we chose not to grow Li dendrites directly onto the bare Cu grid, as this would make it difficult to obtain Li dendrites that had the same orientation as the tilt axis.

The diameters of the dendrites were around 100-200 nm. Dendrites came in various morphologies, including “rod” and “bent” shapes. Distinct 2D shapes were observed for the same “bent” Li metal dendrite imaged at various tilting angles as shown in **Supplementary Movie 1 and 2**. In the tomography reconstruction, to show only the surface SEI layer, a threshold on pixel intensity was imposed to show only the surface of the dendrite. However, it is still challenging to determine the exact shape of the dendrite due to the limited tilt range of the stage. The reconstructed tomograms have elongation and ghost tail artifacts.<sup>38,39</sup>

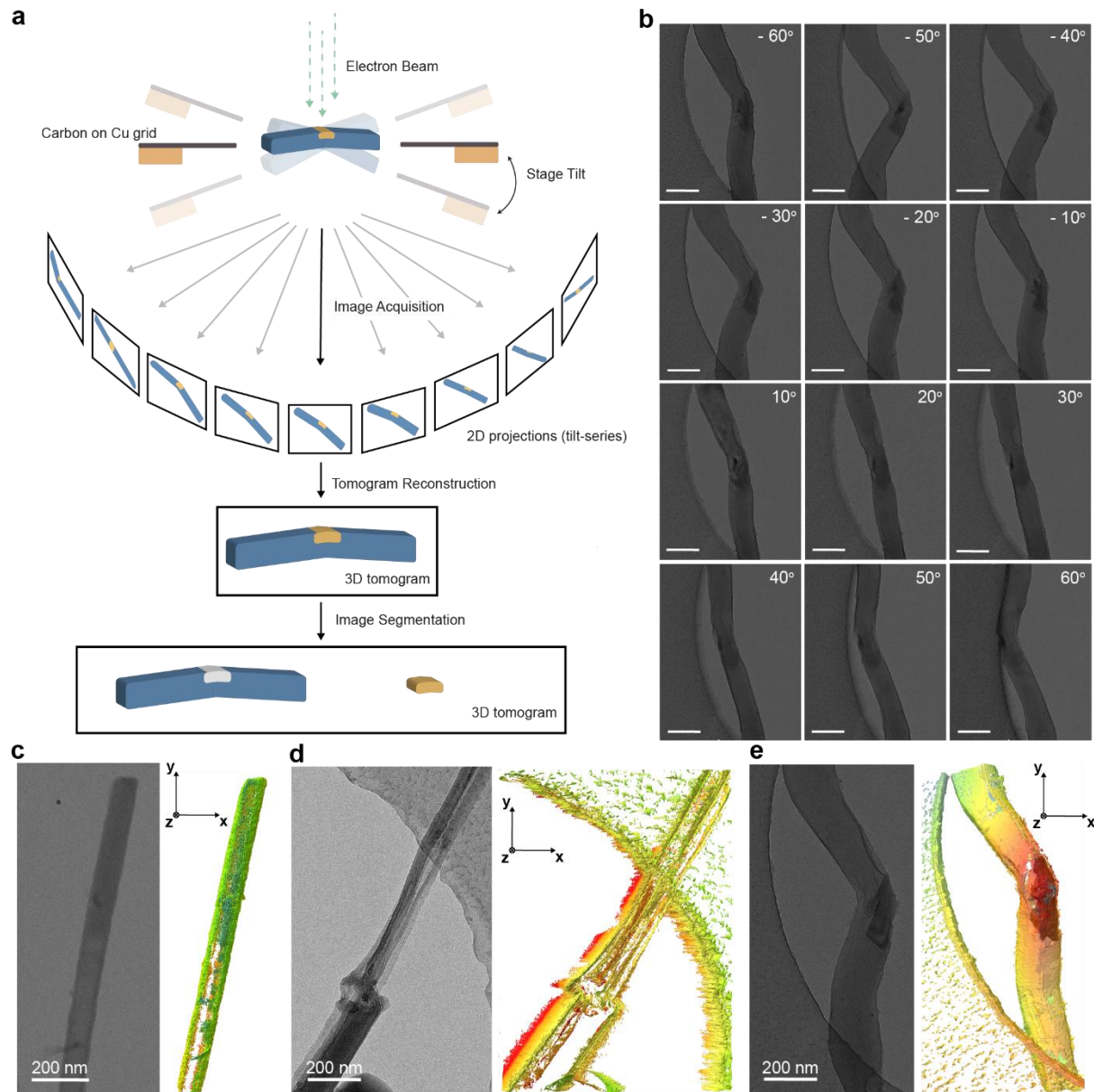


**Fig. 1 | A schematic of cryo-ET, cryo-ET tilt series and corresponding 3D reconstruction of freshly deposited, half-stripped, and calendar aged Li metal dendrites. a, The schematic of cryo-ET data**

collection and image processing procedures. **b**, Cryo-ET tilt series of a Li metal dendrite deposited in 1M LiPF<sub>6</sub> in EC/DEC electrolyte and calendar aged for 24 hours, sampled images shown here for every 10° between -60° to + 60°. The scale bar is 200 nm. **Supplementary Movie 5** shows corresponding full tilt series. **c**, A single image from the tilt series of freshly deposited Li metal dendrite (left panel) and the corresponding 3D representation of reconstructed freshly deposited Li metal dendrite (right panel). The sample was on carbon support. The SEI layer is located on the surface of the Li metal and is highlighted in this display with its color based on the height in z-direction in the reconstruction. **d**, A single image from the tilt series of half-stripped Li metal dendrite (left panel) and the corresponding 3D representation of reconstructed half-stripped Li metal dendrite (right panel). The hollow shell of SEI and remaining Li metal sits on the carbon support. The SEI is colored and highlighted the same way as the freshly deposited sample. **e**, A single image from the tilt series of 24-hour calendar aged Li metal dendrite (left panel) and the corresponding 3D representation of reconstructed calendar aged Li metal dendrite (right panel). The darker contrast region in the cryo-EM image corresponds to LiH. The interface between Li and LiH looks sharp and clear in this projection. The SEI is colored and highlighted the same way as the freshly deposited sample. The LiH particle was annotated separately in white color and overlaid in this dendrite reconstruction to illustrate its spatial disposition. **Supplementary Movie 6** shows the reconstructed calendar aged Li mental dendrite.

In the freshly deposited case, where we immediately disassembled the cells after lithium deposition and the half-stripped case, where we stripped the lithium metal anode halfway, we found that no obvious intraparticle heterogeneity had developed inside the dendrites (**Fig. 1d, e, Supplementary Movie 3**). On the contrary, we observed lithium dendrites with non-uniform contrast in the main body in the case of calendar aging for 24 hours after initial lithium deposition (**Fig. 1e**). The heterogeneity consistently appeared darker throughout the tilt series (**Supplementary Movie 4**) and arose from a difference in the scattering materials in this region. To isolate and analyze this intraparticle heterogeneity, we leveraged convolutional neural networks<sup>40</sup> to do image segmentation and automatically identify the heterogeneity region in the reconstructed tomograms (**Fig. 1e**).

To identify these heterogeneities inside the lithium metal dendrites, we used high-resolution cryo-EM to obtain atomic resolution crystalline lattice images of these regions down specific axes. For the darker contrast region closely interfaced with Li, the lattice spacings were 2.05 Å and 2.35 Å, matching well with LiH (200) and (111) planes, respectively (**Fig. 2a**). The LiH heterogeneity developed here was a single crystal (**Fig. 2b**). The darker contrast of LiH compared to Li in the bright field imaging mode is in accordance with a higher gravimetric density (LiH: 0.78 g cm<sup>-3</sup>, Li: 0.53 g cm<sup>-3</sup>). Furthermore, we captured the atomically sharp interface between Li metal and LiH. Note that this sharp interface does not imply that the entire interface extends toward the viewer in 3D as a sharp plane. In fact, this interface is irregular in 3D (**Fig. 2g-h**). The interface between Li and LiH is along Li (110) with lattice spacing of 2.44 Å and LiH (111) with lattice spacing of 2.35 Å (**Fig. 2c**). We conclude that LiH is the intraparticle heterogeneity that develops inside the Li metal dendrites upon calendar aging but is absent in the freshly deposited samples. This was consistent with our previous reports on not finding the LiH in freshly deposited

samples<sup>20,41</sup>, and suggested a LiH growth mechanism where LiH nucleation and growth happened after initial Li metal deposition, due to gradual accumulation of active hydrogen containing species and its slow diffusion through the SEI layer. If excessive water contamination exists in the electrolyte, such a process could potentially be accelerated to form more LiH during Li metal deposition due to high reactivity of hydrogen in water molecules<sup>42</sup>.

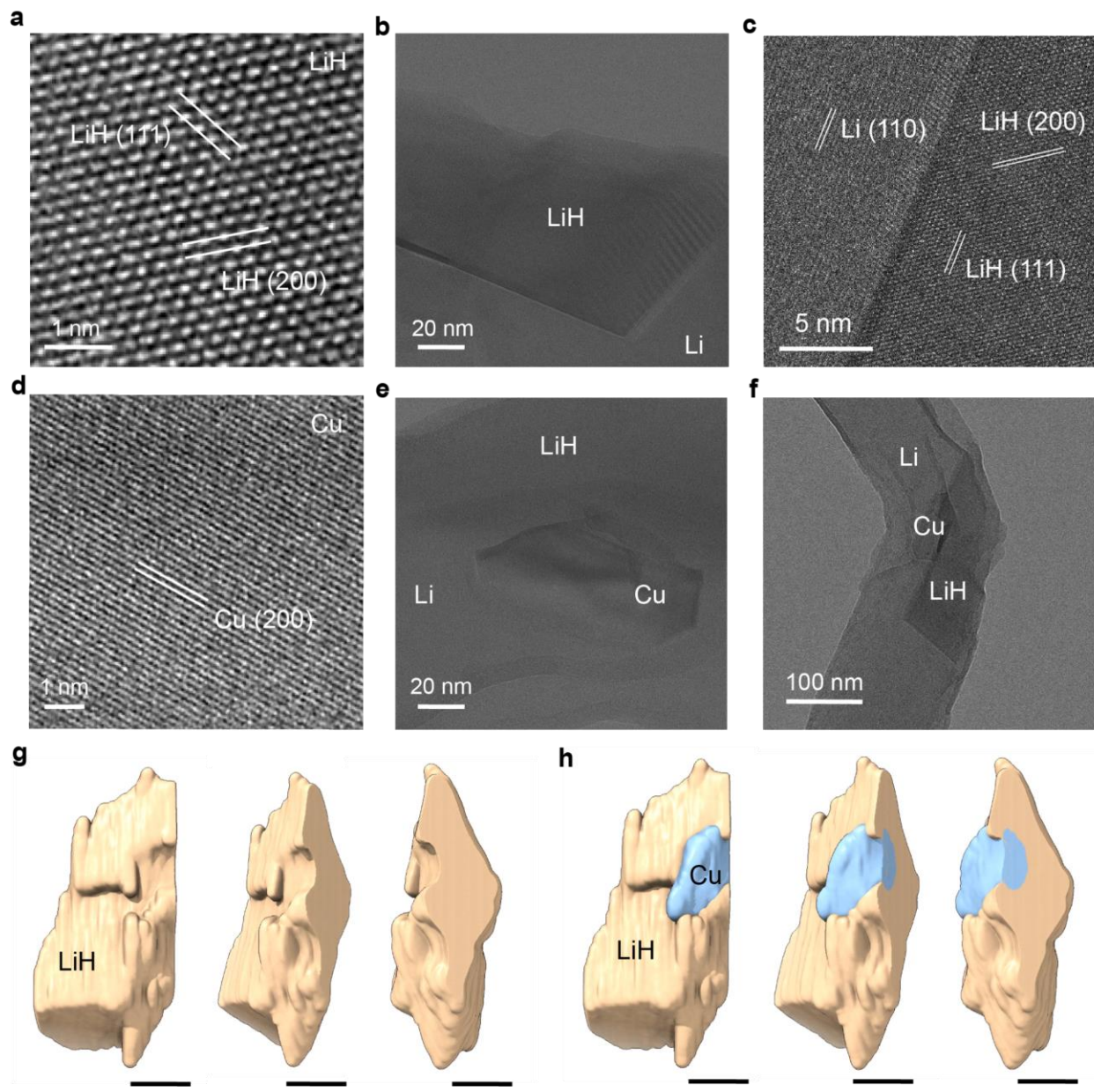


**Fig. 2 | High-resolution cryo-EM images of LiH, Li-LiH interface, Cu nanoparticle, and corresponding 3D reconstructions.** **a**, Atomic resolution image of LiH particle lattice. **b**, Cryo-EM image of LiH heterogeneity arrangement in the Li metal dendrite. **c**, Atomic resolution image of Li-LiH interface inside the Li metal dendrite. FFT of **c** is shown in **Supplementary Fig. 1**. **d**, Atomic resolution image of the embedded Cu nanoparticle lattice. **e**, Cryo-EM image of Cu heterogeneity arrangement in the Li metal

dendrite. **f**, A 2D view of Li, LiH, and Cu arrangement in the Li metal dendrite. **g**, The 3D reconstruction of LiH alone. Three views from different angles of the reconstructed LiH particle were presented here. **h**, The 3D reconstruction of LiH together with the Cu nanoparticle. Three corresponding views of the reconstructed LiH-Cu composite were presented here. Note that LiH and Cu particles were segmented separately from the tomograms. The reconstructions of two particles were overlaid together. The scale bar is 100 nm.

To put the atomic details in the context of the aged dendrites, we examine the reconstruction of the LiH clearly showing an irregular “swiss-cheese-like” shape when viewed in 3D from different orientations (**Fig. 2g**, **Supplementary Movies 7, 8**). There is an irregular surface facing the Li metal portion in the dendrite, while the outer surface of LiH extends to the dendrite surface. This LiH particle inside the Li dendrite metal was roughly 100×200 nm in 2D. More interestingly, in the reconstruction, we were able to identify a smaller third region inside the dendrite that was different from Li and LiH, as another heterogeneous particle. This region was closely interfaced with both Li and LiH as shown in the 3D reconstruction (**Supplementary Movies 7, 8**). The lattice spacing of this third region was 1.8 Å which corresponded to Cu (200). This encapsulation indicates that the Cu nanoparticle was picked up during the nucleation and growth of Li metal. The Cu impurity could also be found in the half-stripped case (**Supplementary Movie 3**). Such Cu nanoparticle detachment from the current collectors could lead to inferior battery performance, because metal particle contamination can cause an internal short circuit between the anode and cathode, which leads to a thermal runaway inside the battery<sup>43,44</sup>. The fact that Cu nanoparticles resided in the middle of the dendrite, instead of the tip or the base, supported the coexistence of the basal and the tip growth modes in the Li metal dendrite growth. Otherwise, the particle would be either at the tip in the case of basal growth or at the base in the case of tip growth<sup>45</sup>. Cu nanoparticles can be found in either fresh or calendar aged dendrites. However, there is not a necessary causal relationship between Cu nanoparticle existence and LiH growth as can be seen from a later case where there was no Cu nanoparticle but still significant LiH growth inside Li metal dendrites. The spatially close interface between LiH and Cu suggests that the strained area inside the Li metal can be a preferred location for heterogeneous phase nucleation, and the convex surface of the Cu nanoparticle further lowered the nucleation barrier of LiH.

To understand how LiH intraparticle heterogeneity develops as aging progresses, we further extended the calendar aging to a week for the Li metal anode sample before cryo-ET sample preparation. The same tomographic reconstruction and segmentation pipeline was used. The tilt series and 3D reconstruction are shown in **Fig. 3a**. There were three major differences compared with the 24-hour aged sample. First, the SEI surface of the dendrite became rougher and thicker. Second, there were porous clusters of SEIs attached to the dendrite surface (**Fig. 3b, c**). Both observations are consistent with previous reports about the growth of SEI on aged carbonaceous anodes and Li metal anodes, where these agglomerates make up the extended SEI<sup>34,35</sup>. These porous clusters that make up the extended SEI expanded up to over 100 nm in thickness. Third, in the one-week aged sample, the LiH took up a much larger portion of the dendrite compared with

the 24-hour aged sample, which indicated a continuous growth of LiH upon aging (**Fig. 3b**). The LiH remained single-crystalline after extended aging for a week.

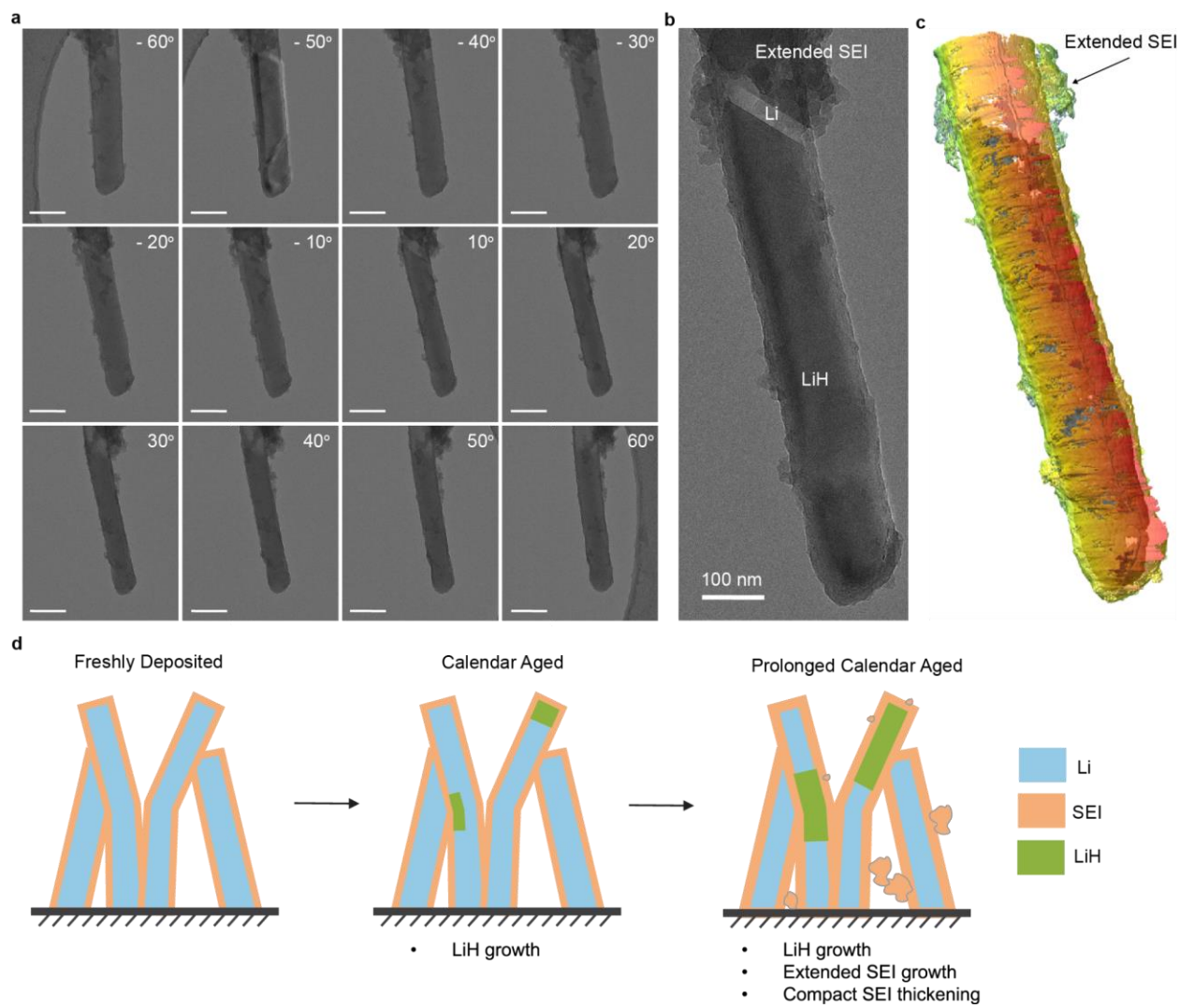


**Fig. 3 | Cryo-ET tilt series and corresponding 3D reconstructions of a 7-day calendar aged Li metal dendrite.** **a**, Cryo-ET tilt series of a Li metal dendrite calendar aged for 7 days, sampled images shown here for every 10° between -60° to + 60°. The scale bar is 200 nm. **Supplementary Movie 9** shows corresponding full tilt series. **b**, A cryo-EM image of a 7-day calendar aged Li metal dendrite. The darker contrast region inside the dendrite body corresponds to LiH. The porous layer outside the Li metal portion corresponds to the extended SEI. The interface between Li and LiH is sharp and clear as well. **c**, The 3D representation of reconstructed calendar aged Li metal dendrite with the same visualization and segmentation of SEI and LiH as shown in **Fig. 1**. **Supplementary Movie 10** shows 3D view of reconstructed Li metal dendrite aged for 7 days. **d**, The schematic illustrations of fresh and aging Li metal anodes, showing the temporal and spatial separation of LiH and extended SEI growth.

Note that the growth of extended SEI is another source of lithium inventory loss aside from the LiH formation during the aging process. The reactive Li metal might lose electrons to partially reduced species in the swollen SEI and such processes would generate reactive hydrogen containing species to either react with Li metal to form LiH or diffuse into bulk electrolyte and initiate extended SEI growth. However, we observed a clear spatial separation between extended SEI growth and LiH growth. Although some extended SEI growth occurred on the LiH surface, the majority of the heavy extended SEI growth was on the remaining Li metal surface. This spatial separation was interesting. On one hand, it suggested that the extended SEI growth was unlikely the result of partially soluble SEI species reprecipitation from the electrolyte, otherwise we would expect more uniform extended SEI distribution on both Li metal and LiH. In addition, it seemed to suggest that extended SEI growth was more of a local phenomenon at the proximity of Li metal surface, and the fact that substantial extended SEI growth was observed only after prolonged calendar aging suggested that there existed also temporal separation between extended SEI growth and LiH growth aside from the spatial separation (**Fig. 3d**). We postulate that a likely scenario would be that LiH nucleation and growth happened faster in the beginning to convert local active Li metal in the dendrite, and progressed towards the other end. At the same time, the original Li metal portion that was far from the LiH nuclei reacted with electrolyte to form extended SEI with a slower rate. As the LiH growth progressed, the extended SEI grew thicker and made it difficult for reactive hydrogen containing species to diffuse to the Li metal surface and to react.

With low-dose cryo-EM, we further examined the compact SEI, the SEI portion that closely interfaced with the anode particle, on LiH surfaces. For the 24-hour calendar aged sample, the compact SEI on the LiH surface was fully amorphous and uniform (**Fig. 4a, c**). It also has a thickness of approximately 10 nm (**Fig. 4b**), similar to that of the SEI on the fresh Li metal surfaces. This indicated that the preferential nucleation of LiH in certain parts of the Li metal dendrite was unlikely the result of a shorter SEI diffusion length for reactive hydrogen containing species to reach the Li metal surface. The interface between SEI and LiH remained sharp and smooth. For the one-week calendar aged sample, the thickness of compact SEI on LiH surface increased by about 2-3 nm, to ~12-14 nm. The SEI, after one-week aging, became rougher while the LiH-SEI interface remained sharp (**Fig. 4e, h**). Notably, a similar amount of increment in SEI thickness was observed for both LiH and Li metal surfaces. Still, the aged SEI on both Li metal and LiH remained amorphous (**Fig. 4f, i**). The extended SEI showed lighter contrast compared to the compact SEI, which is consistent with the previous report that extended SEI were mostly organic species from electrolyte decomposition<sup>35</sup>.

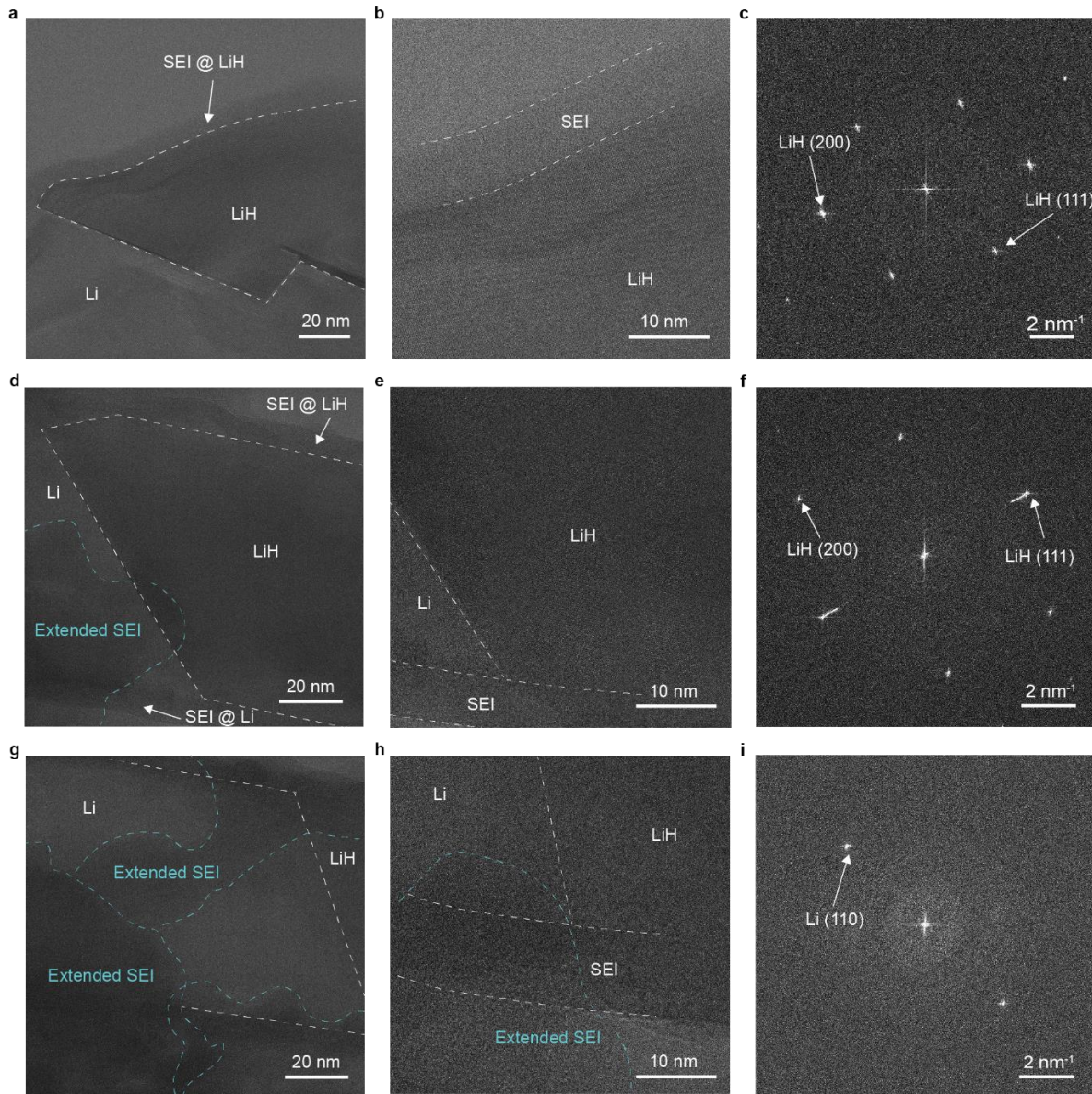


**Fig. 4 | High-resolution cryo-EM images of SEI and extended SEI on calendar aged Li metal dendrites.**

**a**, Overall morphology of SEI on LiH portion in a Li metal dendrite calendar aged for 1 day. **b**, A zoomed-in view of SEI on LiH in a 1-day calendar aged Li metal dendrite. SEI on LiH was fully amorphous. **c**, Fast Fourier Transform (FFT) image of **b**. The only reflections correspond to LiH (111) and LiH (200) lattice spacings, showing that SEI on LiH was amorphous. **d**, Overall morphology of SEI on LiH portion and extended SEI growth on Li metal portion in a Li metal dendrite calendar aged for 7 days. The sample was tilted to show the LiH lattices. **e**, A zoomed-in view of compact SEI on LiH. SEI on LiH in the prolonged calendar aging was fully amorphous. **f**, FFT image of **e**. The only reflections correspond to LiH (111) and LiH (200) lattice spacing. **g**, Another view of SEI on LiH portion and extended SEI growth on Li metal portion in a Li metal dendrite calendar aged for 7 days. The sample was tilted to show the Li metal lattices. **h**, A zoomed-in view of extended SEI on Li and compact SEI on LiH in a 7-day calendar aged Li metal dendrite. **i**, FFT image of **h**. The only reflection corresponds to Li (110).

## Conclusions

By capitalizing on recent advancements in cryo-EM and cryo-ET, we elucidated the structural and compositional changes in calendar aged Li metal anodes where we reconstructed a 3D representation of the deposited Li metal dendrites. During the calendar aging process, we observed two aging phenomena: the growth of LiH and the growth of extended SEI. We identified both temporal and spatial separation of these two phenomena in Li metal anode aging. In shorter-term calendar aging, we only noted the growth of LiH; in prolonged calendar aging, we observed more extensive LiH growth accompanied by the growth of the extended SEI. Specifically, a majority of the extended SEI was found to be spatially associated with the Li metal portion within the dendrite, while only limited extended SEI was observed on the LiH portion. By employing a combination of multiscale imaging and diffraction capabilities, we achieved atomic-level resolution images of LiH intraparticle heterogeneities and of the interfaces between Li and LiH. Although we cannot exclude the possibility of SEI dissolution and precipitation mechanisms contributing to extended SEI growth on the LiH portion, the predominant presence of extended SEI on the Li metal portion suggests that its growth occurs mostly locally. Our temporal and spatial differentiations of LiH and extended SEI growth provide valuable insights into understanding reaction kinetics in distinct Li metal anode aging modes. Moreover, these findings offer potential guidelines for mitigation strategies, such as electrolyte design, aimed at controlling and optimizing Li metal batteries. With improved instrumentation, we will be able to further increase the resolution to resolve the spatial arrangements of organic and inorganic domains in the SEI and their corresponding 3D spatial distributions. The establishment of correlation between intraparticle heterogeneity development, interfacial structures, and battery performance will provide tremendous opportunities to decipher otherwise inaccessible spatial and temporal scales of battery degradation mechanisms. The integration of multiscale imaging and three-dimensional tomography has significantly expanded the scope of our analysis, enabling these crucial insights.

## Supplementary Information

### Materials and Methods

The lithium metal deposition was carried out in 2032-type coin-cells. Specifically, both the Li and Cu foils were punched to around  $1.3\text{ cm}^2$  disks. Cu was rinsed with deionized water and acetone prior to transferring to the Ar glove box for coin-cell assembly to remove surface contaminants. The electrolyte, 1 M LiPF<sub>6</sub> in ethylene carbonate and diethylene carbonate (EC/DEC, v 1:1), was stored in argon-filled glove box (Vigor, oxygen <0.01 ppm, water <0.01 ppm). Lithium was mechanically sheared with a polyethylene scraper to remove the surface oxide and improve electrical connection to the stainless-steel coin cell. 60  $\mu\text{L}$  of electrolytes were used in each cell for full wetting of both working and counter electrode surfaces. Li metal plating was carried out on a Biologic VMP3 system. A total capacity of  $0.5\text{ mAh cm}^{-2}$  was deposited under a constant current of  $2\text{ mA cm}^{-2}$ . The half-stripped cells were then discharge at the same current density for  $0.25\text{ mAh cm}^{-2}$ . The cells were then disassembled immediately or rested for different time periods

before disassembly to mimic various cell calendar aging scenarios. After cell disassembly, the deposited Li metal anode was rinsed with pure DEC solvent to remove residual salts, and then sonicated in DEC for 10 s to form a suspension of lithium dendrites in DEC. The lithium dendrites in suspension were then dropped onto the holey carbon grids (Quantifoil, R2/1). The TEM grids were then sealed in an airtight container, which was immediately submerged and crushed in liquid nitrogen to rapidly expose the sample to cryogen without air exposure and preserve the electrolyte and the electrode. The samples were then loaded into cryogenic sample storage boxes under liquid N<sub>2</sub> and transferred into a larger liquid N<sub>2</sub> dewar. For the aging experiments, the cycled cells were rested at open circuit voltage (OCV) for a designated period.

## Instrumentation

All cryo-EM experiments were performed on a Thermo Fisher Titan Krios G3i TEM operated at 300 kV and equipped with an autoloading mechanism located at Stanford SLAC cryo-EM center. Cryo-EM imaging data were acquired by SerialEM with a Gatan K3 direct-detection camera in the electron-counting mode with the Dose-Fractionation function. Electron diffraction patterns were acquired by EPU-D with a CetaD camera.

## Imaging Conditions

Tomography experiments are done at the magnification of 42000X (pixel size = 2.1 Å<sup>2</sup>/pixel) with an electron dose rate of 5 e<sup>-</sup>/Å<sup>2</sup> per tilt image, 120 tilt images range from -60 to +60 degrees, with an accumulated dose ~600 e<sup>-</sup>/Å<sup>2</sup>. The target defocus of the tilt series is 3 μm. HRTEM experiments are done at the magnification of 215000X (pixel size = 0.412 Å<sup>2</sup>/pixel) with an electron dose of 45 e<sup>-</sup>/Å<sup>2</sup> per image. The target defocus is Scherzer defocus in order to obtain high resolution phase contrast. This was achieved by adjusting the defocus value based on a series of short exposures before the final image. Electron diffraction data were collected with a nominal camera length of 680 mm.

## Data processing and visualization

Image stacks from the K3 camera were motion corrected by MotionCor2. The tomograms were reconstructed using IMOD software. The manual annotation of tomograms was done in Thermo Fisher Amira and the automated machine learning based annotation of tomograms were done in EMAN2. The visualization was carried out in ChimeraX. The HRTEM images were analyzed using Gatan GMS software. The HRTEM images were denoised by an Average Background Subtraction Filter (ABSF), which is commonly used in HRTEM to give better results.

## References

1. Lim, J. *et al.* Origin and hysteresis of lithium compositional spatiodynamics within battery primary particles. *Science* **353**, 566–571 (2016).
2. Woodford, W. H., Carter, W. C. & Chiang, Y.-M. Design criteria for electrochemical shock resistant battery electrodes. *Energy Environ. Sci.* **5**, 8014–8024 (2012).

3. Wang, C. S., Wu, G. T., Zhang, X. B., Qi, Z. F. & Li, W. Z. Lithium Insertion in Carbon-Silicon Composite Materials Produced by Mechanical Milling. *J. Electrochem. Soc.* **145**, 2751 (1998).
4. Kasavajjula, U., Wang, C. & Appleby, A. J. Nano- and bulk-silicon-based insertion anodes for lithium-ion secondary cells. *J. Power Sources* **163**, 1003–1039 (2007).
5. Sun, Y., Liu, N. & Cui, Y. Promises and challenges of nanomaterials for lithium-based rechargeable batteries. *Nat. Energy* **1**, 1–12 (2016).
6. Peled, E. & Menkin, S. Review—SEI: Past, Present and Future. *J. Electrochem. Soc.* **164**, A1703–A1719 (2017).
7. Xu, K. Electrolytes and Interphases in Li-Ion Batteries and Beyond. *Chem. Rev.* **114**, 11503–11618 (2014).
8. Birkl, C. R., Roberts, M. R., McTurk, E., Bruce, P. G. & Howey, D. A. Degradation diagnostics for lithium ion cells. *J. Power Sources* **341**, 373–386 (2017).
9. Cannarella, J. & Arnold, C. B. Stress evolution and capacity fade in constrained lithium-ion pouch cells. *J. Power Sources* **245**, 745–751 (2014).
10. Cheng, X. & Pecht, M. In Situ Stress Measurement Techniques on Li-ion Battery Electrodes: A Review. *Energies* **10**, 591 (2017).
11. Blazek, P. *et al.* Axially and radially inhomogeneous swelling in commercial 18650 Li-ion battery cells. *J. Energy Storage* **52**, 104563 (2022).
12. Aiken, C. P. *et al.* A Survey of In Situ Gas Evolution during High Voltage Formation in Li-Ion Pouch Cells. *J. Electrochem. Soc.* **162**, A760 (2015).
13. Pinson, M. B. & Bazant, M. Z. Theory of SEI Formation in Rechargeable Batteries: Capacity Fade, Accelerated Aging and Lifetime Prediction. *J. Electrochem. Soc.* **160**, A243–A250 (2013).
14. Metzger, M., Strehle, B., Solchenbach, S. & Gasteiger, H. A. Origin of H<sub>2</sub> Evolution in LIBs: H<sub>2</sub>O Reduction vs. Electrolyte Oxidation. *J. Electrochem. Soc.* **163**, A798 (2016).
15. Berkes, B. B., Schiele, A., Sommer, H., Brezesinski, T. & Janek, J. On the gassing behavior of lithium-ion batteries with NCM523 cathodes. *J. Solid State Electrochem.* **20**, 2961–2967 (2016).
16. Ellis, L. D. *et al.* Quantifying, Understanding and Evaluating the Effects of Gas Consumption in Lithium-Ion Cells. *J. Electrochem. Soc.* **164**, A3518 (2017).
17. Aurbach, D. & Weissman, I. On the possibility of LiH formation on Li surfaces in wet electrolyte solutions. *Electrochem. Commun.* **1**, 324–331 (1999).
18. Li, Y., Huang, W., Li, Y., Chiu, W. & Cui, Y. Opportunities for Cryogenic Electron Microscopy in Materials Science and Nanoscience. *ACS Nano* **14**, 9263–9276 (2020).
19. Zhang, Z. *et al.* Cryogenic Electron Microscopy for Energy Materials. *Acc. Chem. Res.* **54**, 3505–3517 (2021).
20. Li, Y. *et al.* Atomic structure of sensitive battery materials and interfaces revealed by cryo-electron microscopy. *Science* **358**, 506–510 (2017).

21. Zachman, M. J., Tu, Z., Choudhury, S., Archer, L. A. & Kourkoutis, L. F. Cryo-STEM mapping of solid–liquid interfaces and dendrites in lithium-metal batteries. *Nature* **560**, 345–349 (2018).
22. Shadik, Z. *et al.* Identification of LiH and nanocrystalline LiF in the solid–electrolyte interphase of lithium metal anodes. *Nat. Nanotechnol.* **16**, 549–554 (2021).
23. Xu, G. *et al.* The Formation/Decomposition Equilibrium of LiH and its Contribution on Anode Failure in Practical Lithium Metal Batteries. *Angew. Chem. Int. Ed.* **60**, 7770–7776 (2021).
24. Xiang, Y. *et al.* Quantitatively analyzing the failure processes of rechargeable Li metal batteries. *Sci. Adv.* **7**, eabj3423 (2021).
25. Scharf, J. *et al.* Bridging nano- and microscale X-ray tomography for battery research by leveraging artificial intelligence. *Nat. Nanotechnol.* **17**, 446–459 (2022).
26. Heenan, T. M. M., Tan, C., Hack, J., Brett, D. J. L. & Shearing, P. R. Developments in X-ray tomography characterization for electrochemical devices. *Mater. Today* **31**, 69–85 (2019).
27. Zenyuk, I. V. Bridging X-ray computed tomography and computational modeling for electrochemical energy-conversion and –storage. *Curr. Opin. Electrochem.* **13**, 78–85 (2019).
28. Yu, Z., Wang, J. & Liu, Y. High-dimensional and high-resolution x-ray tomography for energy materials science. *MRS Bull.* **45**, 283–289 (2020).
29. Li, J. *et al.* Dynamics of particle network in composite battery cathodes. *Science* **376**, 517–521 (2022).
30. Pietsch, P. & Wood, V. X-Ray Tomography for Lithium Ion Battery Research: A Practical Guide. *Annu. Rev. Mater. Res.* **47**, 451–479 (2017).
31. Withers, P. J. *et al.* X-ray computed tomography. *Nat. Rev. Methods Primer* **1**, 1–21 (2021).
32. Midgley, P. A. & Dunin-Borkowski, R. E. Electron tomography and holography in materials science. *Nat. Mater.* **8**, 271–280 (2009).
33. Scott, M. C. *et al.* Electron tomography at 2.4-ångström resolution. *Nature* **483**, 444–447 (2012).
34. Boyle, D. T. *et al.* Corrosion of lithium metal anodes during calendar ageing and its microscopic origins. *Nat. Energy* **6**, 487–494 (2021).
35. Huang, W. *et al.* Evolution of the Solid–Electrolyte Interphase on Carbonaceous Anodes Visualized by Atomic-Resolution Cryogenic Electron Microscopy. *Nano Lett.* **19**, 5140–5148 (2019).
36. Li, Y. *et al.* Correlating Structure and Function of Battery Interphases at Atomic Resolution Using Cryoelectron Microscopy. *Joule* **2**, 2167–2177 (2018).
37. Radermacher, M. Weighted Back-projection Methods. in *Electron Tomography: Methods for Three-Dimensional Visualization of Structures in the Cell* (ed. Frank, J.) 245–273 (Springer, New York, NY, 2006). doi:10.1007/978-0-387-69008-7\_9.
38. Turk, M. & Baumeister, W. The promise and the challenges of cryo-electron tomography. *FEBS Lett.* **594**, 3243–3261 (2020).

39. Frangakis, A. S. & Förster, F. Computational exploration of structural information from cryo-electron tomograms. *Curr. Opin. Struct. Biol.* **14**, 325–331 (2004).
40. Chen, M. *et al.* Convolutional neural networks for automated annotation of cellular cryo-electron tomograms. *Nat. Methods* **14**, 983–985 (2017).
41. Zhang, Z. *et al.* Capturing the swelling of solid-electrolyte interphase in lithium metal batteries. *Science* **375**, 66–70 (2022).
42. Vilá, R. A. *et al.* LiH formation and its impact on Li batteries revealed by cryogenic electron microscopy. *Sci. Adv.* **9**, eadf3609 (2023).
43. Sun, Y. *et al.* A comprehensive research on internal short circuits caused by copper particle contaminants on cathode in lithium-ion batteries. *eTransportation* **13**, 100183 (2022).
44. Huang, L. *et al.* A review of the internal short circuit mechanism in lithium-ion batteries: Inducement, detection and prevention. *Int. J. Energy Res.* **45**, 15797–15831 (2021).
45. Um, J. H. & Yu, S.-H. Unraveling the Mechanisms of Lithium Metal Plating/Stripping via In Situ/Operando Analytical Techniques. *Adv. Energy Mater.* **11**, 2003004 (2021).

### Acknowledgements

Y.C and W.C. acknowledge the CryoEM research support from the Department of Energy, Office of Basic Energy Sciences, Division of Materials Science and Engineering under contract DE-AC02-76SF00515. Z.Z. acknowledges support by Stanford Interdisciplinary Graduate Fellowship. W.Z. acknowledges support by Stanford Interdisciplinary Graduate Fellowship. We acknowledge the use and support of the Stanford-SLAC CryoEM Facilities. Part of this work was performed at the Stanford Nano Shared Facilities (SNSF) and Stanford Nanofabrication Facility (SNF), supported by the National Science Foundation under award ECCS-2026822.

### Author contributions

Z.Z., Y.L., W.C. and Y.C. conceived the project and designed the experiments. Z.Z. performed electrochemical experiments. Z.Z., Y.L., and W.Z. carried out cryo-EM and cryo-ET experiments. W. Z., G. W., and M. S. performed 3D visualization. J.W. and Y.Y. helped with electrochemical measurements. Z.Z., W.C., and Y.C. co-wrote the manuscript. All authors discussed the results and contributed to the completion of the manuscript.

### Competing interests

Authors declare that they have no competing interests.